AFGC-ACI-*fib*-RILEM Int. Symposium on Ultra-High Performance Fibre-Reinforced Concrete,
UHPFRC 2017 – October 2-4, 2017, Montpellier, France

A NUMERICAL MODEL TO DETERMINE THE CHARACTERISTIC LENGTH OF UHPFRC BEAMS

Philipp Hadl (1) and Nguyen-Viet Tue (1)

(1) Institute of Structural Concrete, Graz University of Technology, Austria

Abstract

This paper presents a numerical approach to determine the characteristic length of UHPFRC beams. In principle, the model calculates force or flexural-tensile stress – mid-span deflection relationships of 4-point-bending tests. Since each fibre is considered separately in the model, the position to the crack as well as the embedded length and angle are known for each fibre. By iterative calculation of the compression zone height, the cross-sectional load bearing capacity can be determined depending on the given strain plane or crack width. The deflection is calculated with the principle of virtual work by double integration of the curvatures over the length of the prism. Consequently, the characteristic length is determined for each bending beam by comparison with experimental results. By this mean, associated stress-strain relationships are derived from bending tests. In addition, the influence of scattering in the fibre distribution and orientation on the load bearing behaviour has been investigated.

Résumé

Cet article présente une approche numérique afin de déterminer la longueur caractéristique des poutres en BFUP. En principe le modèle calcule la force ou la contrainte équivalente en flexion en fonction de la flèche à mi-portée dans un essai de flexion 4 points. Dans la mesure où chaque fibre est considérée séparément dans le modèle, la position par rapport aux fissures ainsi que les angles et longueurs ancrées sont connus pour chaque fibre. Par des calculs itératifs de la hauteur de la zone comprimée, la capacité résistante de la section peut être déterminée en fonction de la pente du diagramme de déformation ou de l'ouverture de fissure que l'on se donne. La flèche est calculée par le principe du travail virtuel par double intégration des courbures le long du prisme. En conséquence, la longueur caractéristique est déterminée pour chaque poutre testée en flexion par comparaison avec les résultats expérimentaux. Ainsi, des relations contrainte-déformation se déduisent des essais de flexion. De plus, l'influence de la dispersion dans la répartition et l'orientation des fibres sur la capacité résistante a pu être étudiée.

1. INTRODUCTION

For the design of UHPFRC structures reliable knowledge about the tensile stress-strain response is fundamental. If flexural test methods are used to assess this constitutive property, inverse analysis is required to quantify the intrinsic tensile behaviour.

In bending tests, a discrete macro-crack, similar to a plastic hinge, is formed after exceeding the peak load. In the area of the plastic hinge the curvatures increase disproportionately along the characteristic length l_{ch}. Consequently, the hypothesis of Navier/Bernoulli is no longer valid and the cross-section does not remain plane. Therefore, the crack width in the unloading branch has to be converted to a tensile strain by the definition of a characteristic length $\varepsilon_t = w_{cr} / l_{ch}$ (see crack-band-model [1]). According to [2], l_{ch} depends on a multitude of factors, such as component and compressive zone height, cross-section, load factor and bending moment. In Figure 1 the area of localization and the characteristic length are shown schematically.

Since the characteristic length has a non-linear profile, l_{ch} is replaced by a reduced length with constant curvature (here called l_{local}) and same size. This simplified definition of the characteristic length is used in the model presented below.

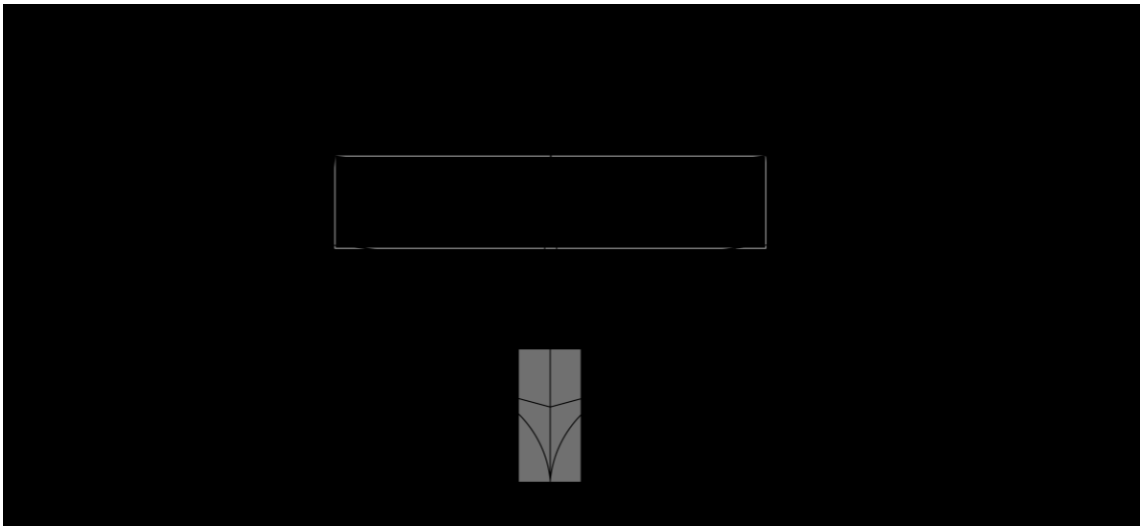

Figure 1: Definition of the characteristic length [2]

So far, there is no uniform definition of the exact length of l_{local} and the values in literature differ in a wide range. While l_{local} is specified with $2/3 \cdot h$ in the French [3] and Swiss UHPFRC guidelines [3], [4] defines a value of $2 \cdot h$. The Japanese guideline [6] also describes an approach depending on the cross-section height. An overview of different approaches is published in [2] and [7] for instance.

2. MODEL DESCRIPTION

The numerical model calculates force or flexural tensile strength - mid-span defection relationships of 4-point-bending tests and associated constitutive laws. It can be used for beams with deflection-softening and deflection-hardening behaviour. A detailed model description is presented in [10].

2.1 General considerations

For the positioning of the fibres in space, they are referred on their fibre focus (FSP), as proposed in [7]. Initially, a concrete volume with the form shown in Figure 2 (A) is given for each fibre. It consists of 7 cubes of length a, with FSP in the centre. The elements can be aligned completely dense (see Figure 1 (B)), so that each FSP has an equal, direction-independent partial volume. Other volume forms, such as tetrahedron or balls, cannot be aligned completely dense [9].

The FSPs are located on main layers with distance a, as can be seen in Figure 1 (C). The model gives identical fibre positioning in all three spatial directions, which is required in case of homogeneous fibre distribution.

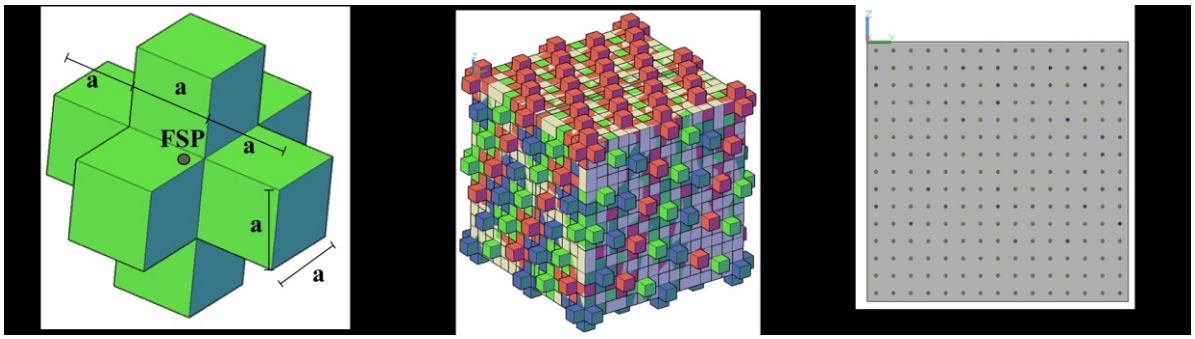

Figure 2: Concrete volume for each fibre (A); reference cube (B); main layers of fibres (C)

The concrete volume of a single fibre $V_{B,EF}$ is calculated by fibre content ρ_f, length l_f, diameter d_f and the specific fibre weight γ_f. Consequently, the distance a between the main layers is determined according to equation 1:

$$a = \sqrt[3]{\frac{V_{B,EF}}{7}} = \sqrt[3]{\frac{\frac{l_f \cdot d_f^2 \cdot \frac{\pi}{4} \cdot \gamma_f}{\rho_f}}{7}} = \sqrt[3]{\frac{l_f \cdot d_f^2 \cdot \pi \cdot \gamma_f}{28 \cdot \rho_f}} \quad (1)$$

In case of a homogeneous fibre distribution each main layer includes the same number of FSPs. If an inhomogeneous fibre distribution is assumed, fibres are positioned by using a Gaussian distribution, a Poisson distribution or by variation of fibre content.

Subsequently fibre orientation is given for each FSP. For this purpose the input of the average fibre orientation η_V and the associated standard deviation $\sigma_{\eta,V}$ is required. According to the test results in [10] and the investigations in [11], $\sigma_{\eta,V}$ is estimated by equation 2. Consequently, the individual values of the fibre orientation are calculated by using a beta distribution in the model.

$$\sigma_{\eta,V} = \frac{4}{\sqrt{12}} \cdot \eta_V \cdot (1 - \eta_V) \quad (2)$$

Depending on the position of the macro-crack, the vertical position as well as the embedded length and angle for each fibre are known, as can be seen in Figure 3. In bending tests and in the model, the load-bearing behaviour is only determined for the longitudinal beam axis.

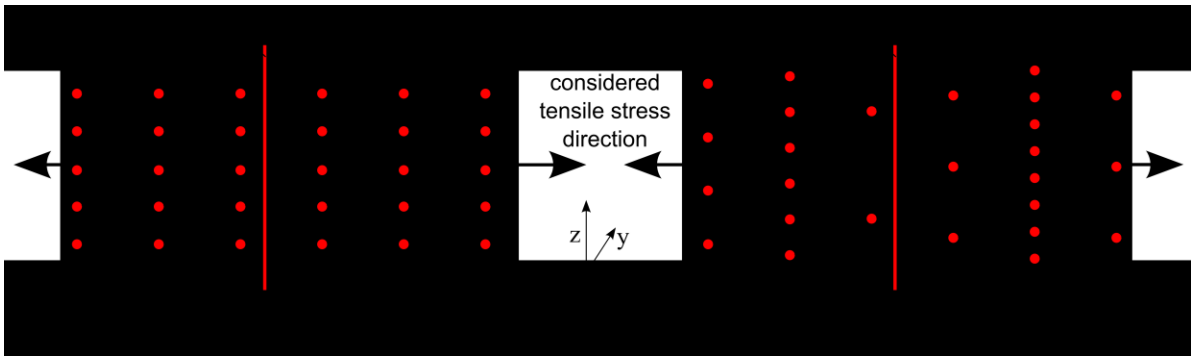

Figure 3: Homogeneous (left) and inhomogeneous fibre distribution (right), fibre orientation and macro-crack position

In order to calculate the fibre forces, an ideal-plastic bond-relationship between fibre and matrix is assumed for UHPC, as proposed in [12] and [13]. The bond strength τ_0 is an input parameter, when the fibre is orthogonal to the crack (inclination angle 0°). Subsequently, the bond strengths for fibres with 15, 30, 45, 60 and 70.53° inclination angle are defined, as described in [10]. Linear interpolation is performed between the individual values. Fibres with inclination angles larger than 70.53° are defined as not effective.

The aggregate interlock of fibreless UHPC is considered as described in [14]. The fracture energy G_f has been investigated in [15] and determined to about 60 N/m for fine grained and about 90 N/m for coarse aggregate UHPC without fibres. In the model the value G_f is an input parameter and has to be defined for each specimen separately.

2.2 Input parameters

The required input parameters are demonstrated in Table 1. In addition to material input parameters the definition of the beam geometry is necessary. Further, input of the flexural tensile strength - mid-span deflection relationship obtained in the experiment is required.

Table 1: Input parameters

cylindrical compressive strength $f_{c,cyl}$	
elastic modulus of UHPC E_{cm}	
tensile matrix strength $f_{ct,0}$	
fracture energy of fibreless UHPC G_f	
fibre length l_f and diameter d_f	
elastic modulus of fibres E_f	
fibre content ρ_f	
bond strength τ_0	
tensile fibre strength f_{ym}	average fibre orientation in the volume η_V
mid-span deflection at peak-load $\delta_{max.}$	flexural tensile strength at peak-load $\sigma_{max.,eq.}=M/W$

2.3 Hardening phase – multiple-cracking

The presented model divides the load bearing behaviour (load-deformation behaviour) of bending beams in three phases, which are shown in Figure 4. Phase I represents the quasi-linear-elastic behaviour until the tensile matrix strength $f_{ct,0}$ is reached (loss of linearity; point 1 in Figure 1). In phase II, multiple cracks are formed, until the peak-load is reached and the failure crack localization occurs in phase III. The softening phase (III) is characterized by fibre pull-out, while the rest of the specimen is unloaded. Phases I and II are summarized in the model description. In case of deflection-softening behaviour, phase II is skipped. Consequently localization and crack-opening starts immediately after the first crack. A detailed description of the load-deformation behaviour of fibre reinforced bending beams is presented in [2] and [16] for instance.

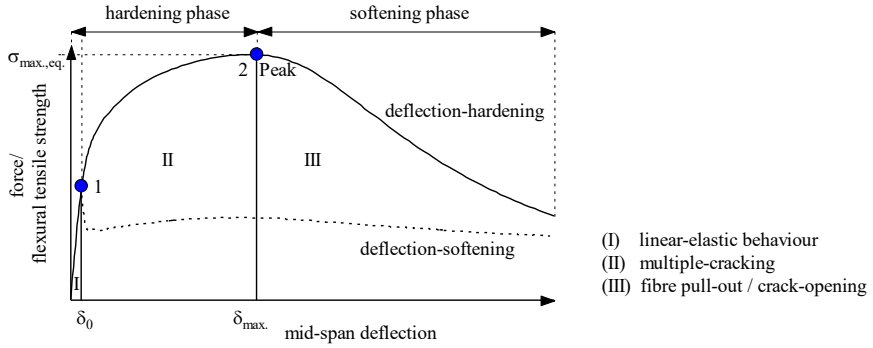

Figure 4: Phases I – III of UHPC bending beams

In order to consider the size effect, the direct tensile matrix strength $f_{ct,0}$ is converted to the flexural matrix strength $f_{ct,fl}$ (nonlinear behaviour initiation point; see Figure 1) by equation 4 [5]. The associated deflection δ_0 is calculated by assuming linear-elastic behaviour.

$$f_{ct,fl} = \frac{f_{ct,0}}{\frac{2 \cdot (h/h_0)^{0.7}}{1 + 2 \cdot (h/h_0)^{0.7}}} \tag{4}$$

During multiple cracking the cross-section remains plane until the peak-load is reached. The results of FE-simulations verify this assumption, as described in [10]. In principle, the mid-span deflection δ is calculated with the principle of virtual work by integrating the curvature and the virtual moment along the beam (double integration of curvature; equation 5). Therefore, the definition $\varkappa$=M/EI is used and the curvature remains constant in the constant bending moment zone. The static and virtual system as well as the curvature for 4-point-bending tests with load introduction at the third points is demonstrated in Figure 5. Similar approaches have been used in [19] and [20] for instance.

$$\delta = \frac{1}{EI} \cdot \int_0^l \overline{M_{(x)}} \cdot M_{(x)} d_x = \int_0^l \overline{M_{(x)}} \cdot \varkappa_{(x)} d_x \tag{5}$$

The curvature at peak-load $\varkappa_P$ is calculated by equation 6, which results from transforming equation 5, according to the approach in [9] ($\delta = \delta_{max.}$; $M_P = \sigma_{max.,eq.} \cdot W$; see input parameters). The exponent k considers the nonlinear curvature distribution between the curvature at crack moment $\varkappa_{cr}$ and $\varkappa_P$. A value of 0.6 is recommended in [16] and used in this investigation.

$$\varkappa_P = \frac{\frac{27\delta}{l_{ef}^2} - \frac{2f_{ct,fl}}{E_{cm}h}\left(\left(\frac{M_{cr}}{M_P}\right)^2 + \frac{1}{2}\left(\frac{M_{cr}}{M_P}\right)^k + \frac{1}{2}\left(\frac{M_{cr}}{M_P}\right)^{k+1} - \left(\frac{M_{cr}}{M_P}\right)^{k+2}\right)}{\left(\frac{M_{cr}}{M_P}\right)^k - \frac{1}{2}\left(\frac{M_{cr}}{M_P}\right)^{k+1} - \frac{1}{2}\left(\frac{M_{cr}}{M_P}\right)^{k+2} + \frac{15}{8}} \quad (6)$$

Figure 5: Determination of the curvature at peak-load according to [16]

The compressive zone height x is determined iteratively with the known curvature $\varkappa_P$ until equilibrium between compressive and tensile forces ($F_c = F_{ct,0} + F_{Rvz} + \Sigma F_{F,i}$) is given in the section. Thereby, $F_{ct,0}$ is the tensile matrix force, F_{Rvz} the force due to aggregate interlock and $\Sigma F_{F,i}$ is the sum of fibre forces. Figure 6 (A) shows the stresses and strains in the section. A linear-elastic material behaviour is used to determine the forces F_c and $F_{ct,0}$.

To determine F_{Rvz}, the definition of a crack width during phase II is required. During loading branch, the crack widths are extremely small, since the crack distance can be assumed to be $s_r \leq l_f$, although crack distances smaller than $l_f/2$ have been observed in [13] and [17]. The crack width at the bottom is defined as $w = \varepsilon_{ctfm} \cdot l_f$. It is significant, that the strain in the crack $\varepsilon_{ct,cr}$ is always twice the average strain ε_{ctfm} ($\varepsilon_{ct,cr} = 2 \cdot \varepsilon_{ctfm}$), due to the constant bond strength (ideal-plastic bond relationship), as can be seen in Figure 6 (B).

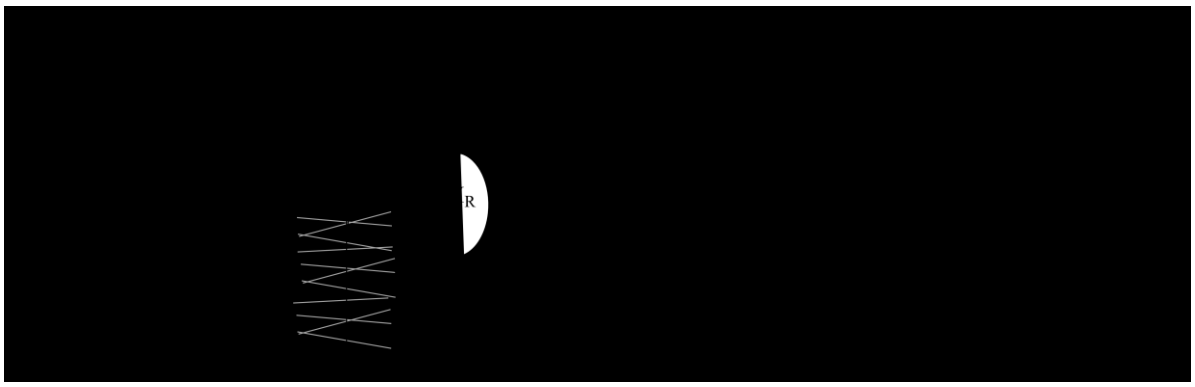

Figure 6: Internal forces at peak-load (left) and strain in the crack $\varepsilon_{ct,cr}$ versus average strain ε_{ctfm} at the bottom (right)

Due to the described positioning of the FSPs, the strain $\varepsilon_{ctf,i,m}$ for each fibre is known. The fibre force $F_{F,i}$ for straight steel fibres is calculated by assuming $\varepsilon_{ct,cr} = 2 \cdot \varepsilon_{ctfm}$ according to equation 7. The fibre force is also limited by the embedded length l_e. Further a possible fibre pull-off has to be considered. Fibre pull-out after activating the fibre force is considered by reducing the embedded length according to the particular crack width depending on the position of each fibre.

$$F_{F,i} = 2 \cdot \varepsilon_{ctf,i,m} \cdot E_f \cdot \frac{d_f^2 \cdot \pi}{4} \leq d_f \cdot \pi \cdot l_e \cdot \tau_i \leq f_y \cdot \frac{d_f^2 \cdot \pi}{4} \quad (7)$$

Since the forces and positions of F_c, $F_{ct,0}$, F_{Rvz} and $\Sigma F_{F,i}$ in the section are known, the moment M_{RP} is calculated. Consequently, the resulting equivalent flexural tensile strength $\sigma_{eq.}=M_{RP}/W$ is determined.

After determination of M_{RP}, additional points between first crack (point 1 in Figure 7) and peak-load (point 2 in Figure 7) are calculated by variation of the curvature $\varkappa_{cr} \leq \varkappa_i \leq \varkappa_P$ and the same procedure. The associated mid-span deflection is calculated according to equation 5. Finally the constitutive law up to peak-load is determined, since strains and stresses are known for each curvature. The strain observed in bending test is directly used for deriving stress-strain relationships, since the cross-section remains plane.

2.4 Softening phase – macro-cracking

The softening phase (phase III in Figure 1) starts after the peak-load has been exceeded in the bending test. Due to the crack opening the deflection is concentrated in the macro-crack and the cross-section does not remain plane. Consequently there is no tensile strain, but a crack opening w_{cr} of the macro-crack. As mentioned above, the crack width is converted to a tensile strain by assuming a characteristic length, according to [1]. By determination of the deflection with the principle of virtual work, an exact definition of l_{local} is possible by comparison with experimental results and considering reversible deformation components.

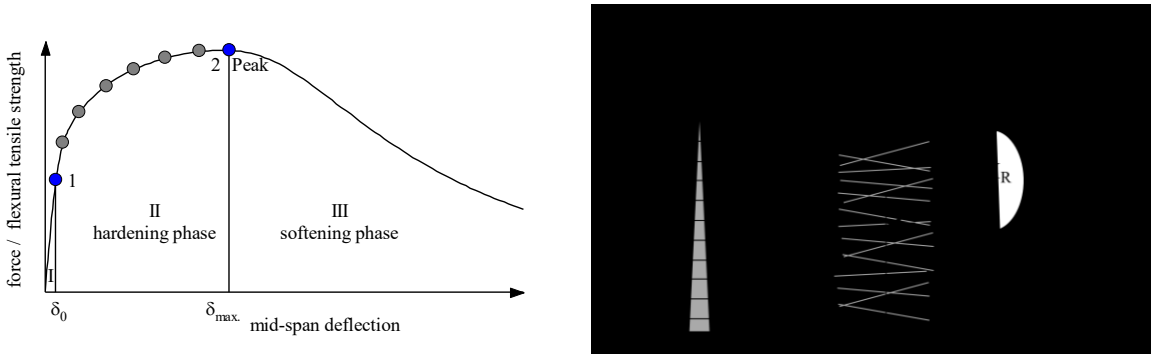

Figure 7: Calculation of additional points between $\varkappa_{cr}$ and $\varkappa_P$ (left) and stresses, strains and crack width in phase III (right; cross-section does not remain plain)

The resultant moment $M_{R,i}$ is calculated for each crack width w_{cr}, since the position of each fibre is known. The compressive zone height and the compressive strain ε_c are determined iteratively until equilibrium between compressive and tensile forces is given in the section ($F_c = F_{ct,0} + F_{Rvz} + \Sigma F_{F,i}$). Figure 7 demonstrates the stresses and strains in the section.

A linear-elastic material behaviour is still used to determine the force F_c and $F_{ct,0}$. In principle, a linear crack path along the cross-section height is assumed, as can be seen in Figure 7. Consequently the forces due to aggregate interlock F_{Rvz} and the fibre forces $\Sigma F_{F,i}$ are defined. Since the crack width $w_{cr,i}$ is known for each fibre the individual fibre forces are determined according to equation 8. However, the required crack width $w_{0,i}$ for fibre activation has to be considered, according to investigations in [13]. Fibre pull-out is considered by reducing the embedded length.

$$F_{F,i} = d_f \cdot \pi \cdot l_e \cdot \tau_i \tag{8}$$

The deflection is calculated by double integration of the curvature along the beam (equation 5). Figure 8 demonstrates the static system, the curvature and the virtual system. The curvature of the compressive zone $\varkappa_{R,LOK,i} = \varepsilon_c / x$ in the area of the localized macro-crack is constant along the entire length l_{local}.

Additionally, reversible deformation components are considered in the calculation of the mid-span deflection. Reversible deformation components occur, since the force in the bending test decreases (unloading), and thus the curvature and deflection in the area beyond the localization reduce. The approach to consider reversible deformations has been described in [10] and has been verified by experimental investigations. In this approach 50 percent of the curvatures beyond the localization area are reversible, if the specimen is totally unloaded. Hence, the curvature $\varkappa_{R,OL,i}$ is always smaller than $\varkappa_P$, as can be seen in Figure 8. Hence, the presented model enables an exact definition of the characteristic length, by comparison with experimental results.

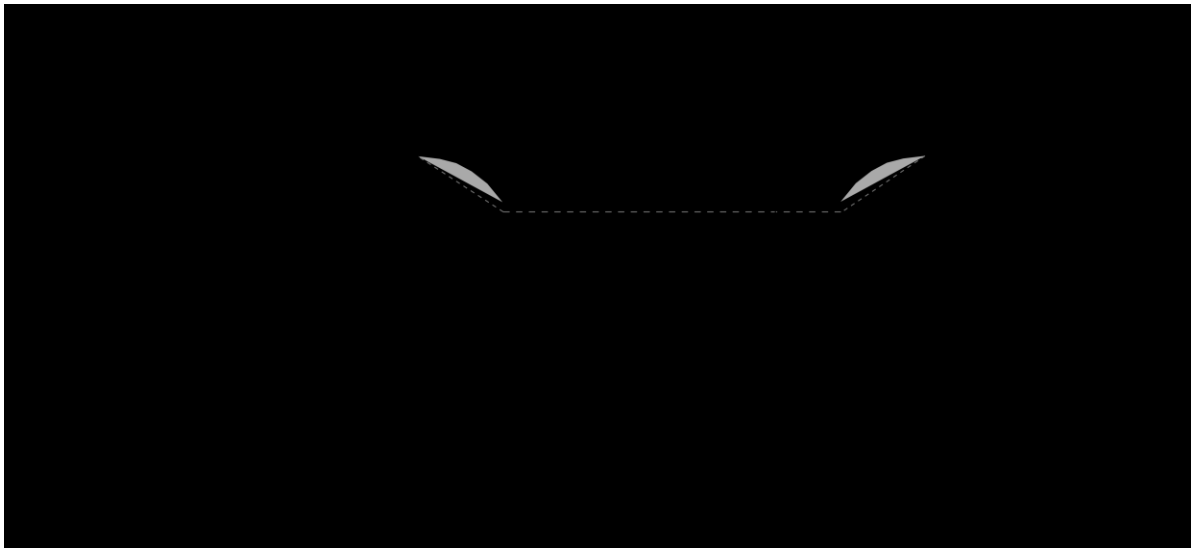

Figure 8: Static system, curvature and virtual system in phase III

The derived stress-strain relationship for the crack-opening phase (unloading branch) is calculated by equation 8. Thereby, the tensile strain $\varepsilon_{ctf,Peak}$ and the crack width $w_P = \varepsilon_{ctf,Peak} \cdot l_f$ due to peak-load have to be considered. Figure 9 shows, for instance, the calculation results for a test specimen with deflection-hardening behaviour.

$$\epsilon_{ctf,i} = \epsilon_{ctf,Peak} + \frac{w_{cr} - w_{Peak}}{l_{local}} \tag{8}$$

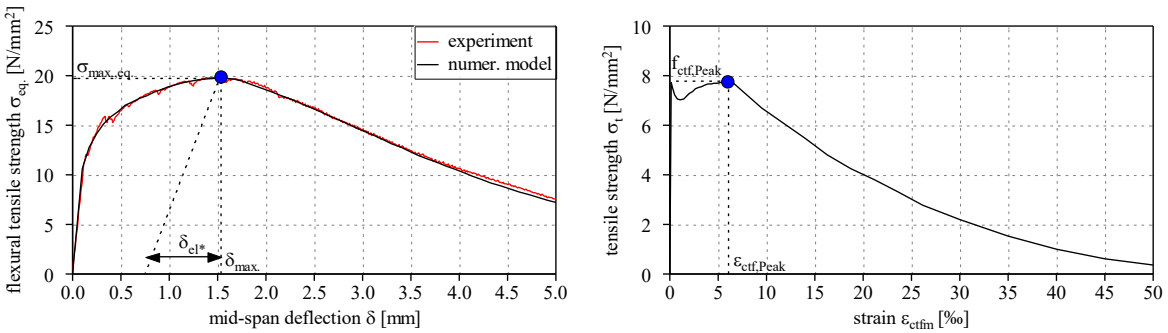

Figure 9: Calculated flexural tensile strength mid-span deflection relationship (left) and associated stress-strain relationship (right)

3. CALCULATION RESULTS

In [16] and [18] extensive experimental investigations on the bending behaviour of fibre reinforced UHPFRC have been conducted. The test program included 4-point-bending tests on standardized beams according to the German guideline for fibre concrete and on thin plates as well as fibre orientation and distribution analysis. The calculation of the mentioned experiments shows excellent correlation both in the area of micro-cracking (phase I + II) and in the area of crack opening (phase III). The used input parameters can be seen in [10].

3.1 Characteristic length

The calculation results demonstrate, that the eccentricity x_r is significant for the unloading branch (phase III), as demonstrated in Figure 10. In addition Figure 10 shows the influence of the characteristic length on the load bearing behaviour in the calculated bending test. If l_{local} is too large, the deflection in phase III will be overestimated. In contrast, if l_{local} is too small, the deflection will be underestimated.

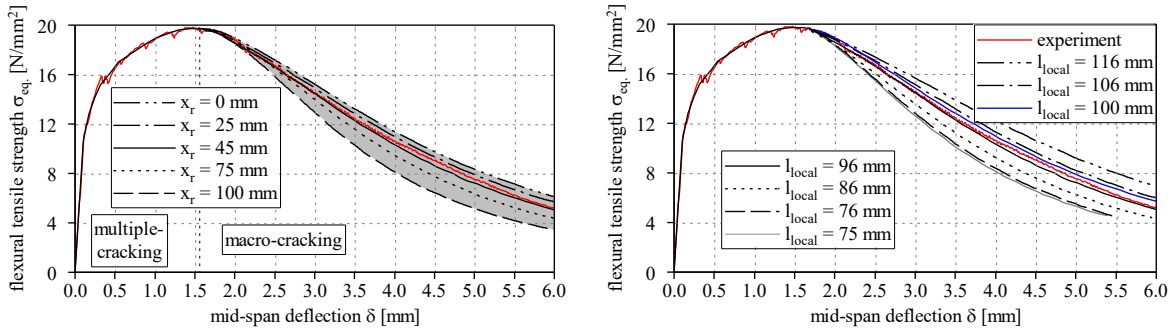

Figure 10: Influence of eccentricity x_r (left) and characteristic length (right) on the calculated flexural tensile strength mid-span deflection relationships

In Figure 11, the determined equivalent flexural tensile strength mid-span deflection relationships are compared with experimental test results in [18]. One representative test is depicted for each fibre content and geometry for both standardized beams (h = 150 mm) and plate specimens (h = 50 mm). Further the determined characteristic length l_{local} is shown as a function of the macro-crack opening w_{cr} - w_P. It is obvious, that l_{local} initially grows with the crack width and approximates a limit value for large crack widths asymptotically.

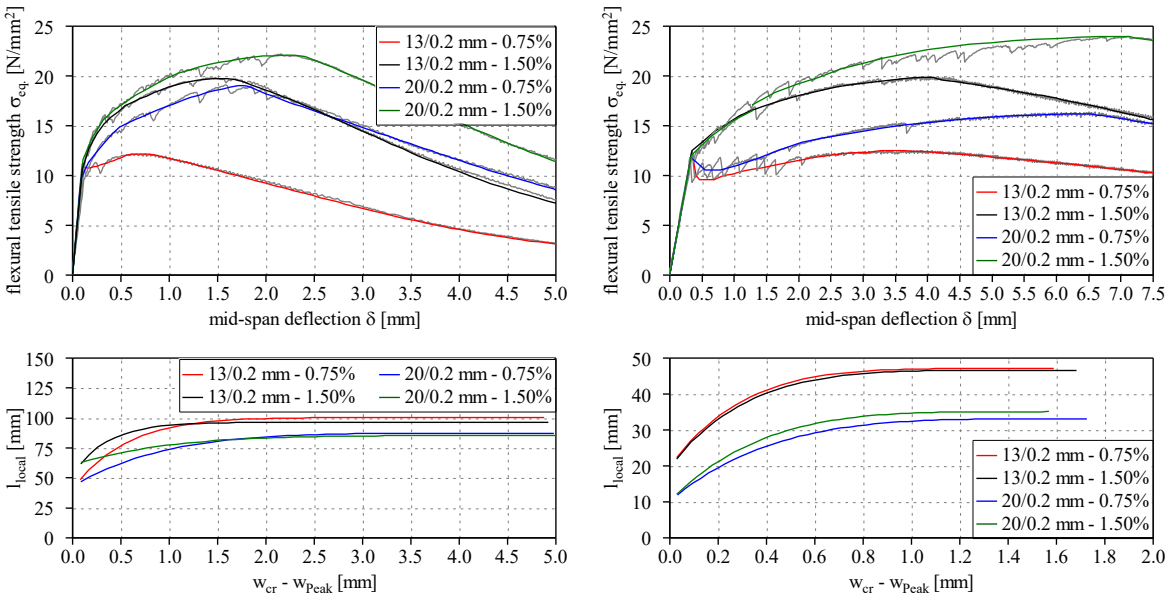

Figure 11: Calculated flexural tensile strength mid-span deflection relationships (top) for standardized beams (left) and plates (right) and characteristic length (bottom)

Figure 12 shows the determined characteristic length achieved by recalculating the experiments in [16] and [18]. It can be seen that the approach according to [3] with 2/3·h overestimates the characteristic length for standardized beams slightly. For plates, this simple approach is assessed as capable. However, the approach of [5] with 2·h is no longer valid.

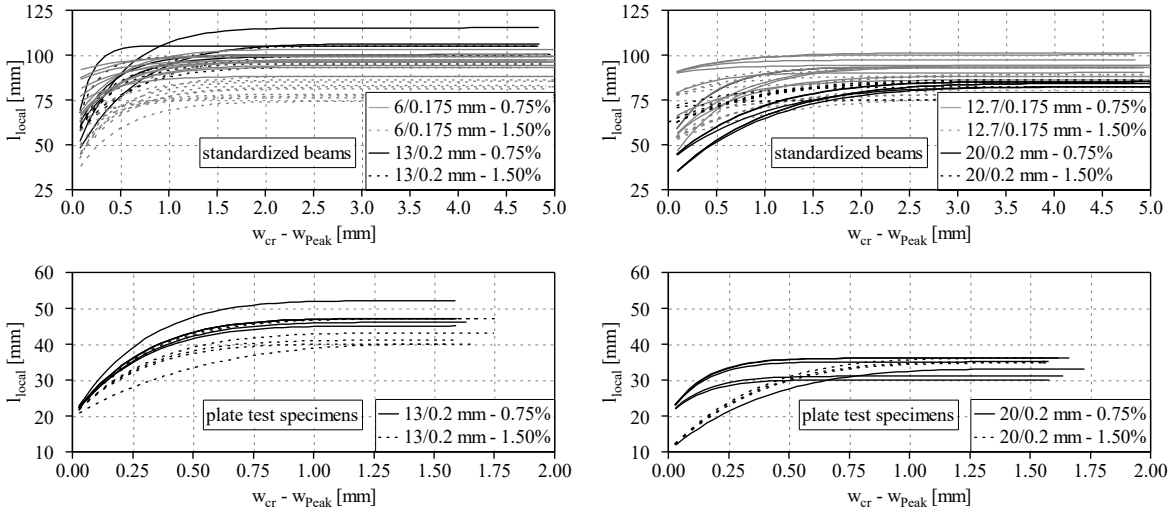

Figure 12: Determined characteristic length for standardized beams (top) and plates (bottom) and different steel fibre contents and geometries

The evaluation of l_{local} for a given tensile strain $\varepsilon_{ct,max}$ of 15, 20 and 25‰ shows that the characteristic length decreases with increasing curvature $\varkappa_P$ at peak-load. Depending on the bending slenderness l_{ef}/h, the curvature $\varkappa_P$ and the beam height, l_{local} can be estimated according to equation 9.

$$l_{local,15/20/25‰} = \frac{2}{3} \cdot h - \frac{h+(25-\varepsilon_{ct,max})\cdot 7.5}{600} \cdot \varkappa_P \qquad \text{for } l_{ef}/h = 4 \tag{9}$$

$$l_{local,15/20/25‰} = \left(h + \left(\varepsilon_{ct,max} - 15\right)\right) - \frac{3}{20} \cdot \varkappa_P \qquad \text{for } l_{ef}/h = 12$$

As expected, the characteristic length strongly depends on the specimen height h and the bending slenderness. Further, the scale effect and the test setup (notched or unnotched beams) have to be considered. If the characteristic length is estimated for the design of UHPFRC structures based on equation 9, is the height of the structural element and not the specimen size. However, test specimens should have similar dimensions (height) as the structural element. For further information, see [10].

3.2 Influence of fibre orientation and distribution

The described positioning of the fibres and the manual input of the average fibre orientation η_V enable the quantification of scattering in the fibre distribution and orientation on the load bearing behaviour. The scattering of the mentioned parameters is simulated by the variation of η_V and the fibre content ρ_f. Figure 13 shows for instance the influence of fibre orientation and distribution on the load bearing behaviour of a standardized beam of UHPC (l_f/d_f = 13/0.2 mm; ρ_f = 1.5 Vol.-%). The curvature at peak-load has been kept constant for these investigations (input of $\sigma_{max.,eq.}$ and $\delta_{max.}$ remain constant). The average fibre orientation η_V varies between 0.55 - 0.65 and 0.50 – 0.70 respectively, the values of ρ_f between 1.375 – 1.625 Vol.-% and 1.25 – 1.75 Vol.-%, which is the same coefficient of variation ($v_{\eta V} = v_{\rho f}$).

The results of the investigations demonstrate, that a scattering in the fibre orientation changes the bending capacity disproportionally ($v_{\sigma,max} \approx 1.2 \cdot v_{\eta V}$). That is because a change in η_V changes both the number of fibres in the section and the fibre orientation in the section. However, a change in the fibre content is completely reflected in the bending behaviour ($v_{\sigma,max} \approx 1.0 \cdot v_{\rho f}$). For further information, see [10].

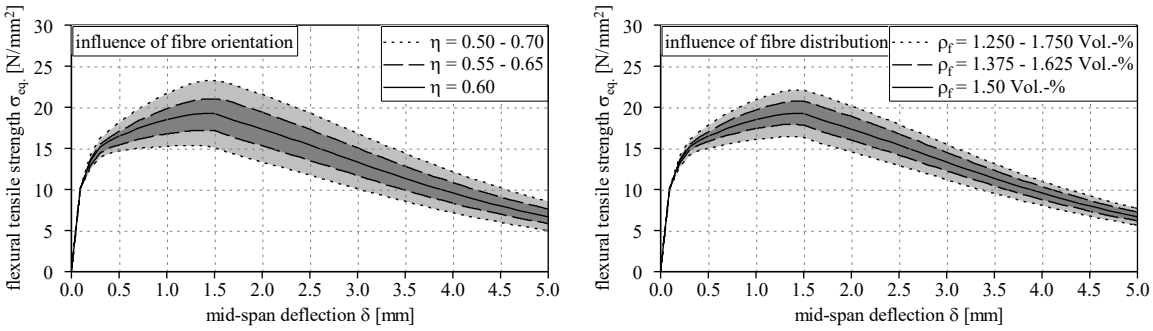

Figure 13: Influence of scattering in fibre orientation and distribution on bending behaviour

4. CONCLUSION

This paper presents a numerical approach to calculate force or flexural tensile strength - mid-span defection relationships of 4-point-bending tests and associated constitutive laws (stress-strain relationships). The load bearing behaviour in the bending test is divided into hardening phase until peak-load is reached and softening phase (crack-opening or fibre pull-out phase). During the unloading branch, the characteristic length is determined for each

bending beam by comparison with experimental results. It has been observed, that the characteristic length initially grows with the crack width and approaches asymptotically a limit value for large crack widths. It slightly decreases for a given strain with increasing curvature at peak-load.

Further the influence of scattering in the fibre distribution and orientation on the load bearing behaviour has been investigated. It was found, that a scattering in the fibre orientation changes the bending capacity disproportionally ($v_{\sigma,max} \approx 1.2 \cdot v_{\eta V}$), while a scattering in the fibre content is completely reflected in the bending behaviour ($v_{\sigma,max} \approx 1.0 \cdot v_{\rho f}$).

REFERENCES

[1] Bazant, S. and Oh, B.-H., 'Crack band theory for fracture of concrete', *Materials and Structures.* **16** (1983) 155-177.
[2] Reichel, M., 'Dünnwandige Segmentfertigteilbauweisen im Brückenbau aus gefasertem UHFB - Tragverhalten, Bemessung und Konstruktion', *PhD-Thesis.* (2010) TU Graz.
[3] AFGC, 'Recommendations Ultra High Performance Fibre Reinforced Concrete', (Setra, 2013).
[4] SIA, 'Ultra-Hochleistungs-Faserbeton (UHFB) – Baustoffe, Bemessung uns Ausführung', (Schweizer Ingenieur und Architektenverein, 2016).
[5] Fehling, E., Schmidt, M., Walraven, J., Leutbecher, T. and Fröhlich, S., 'Ultrahochfester Beton', in 'Betonkalender', 2013 (Ernst & Sohn, Berlin, 2013).
[6] JSCE, 'Recommendations for design and construction of Ultra High Strength Fiber Reinforced Concrete', (Tokyo, 2006).
[7] Habel, K., 'Structural behaviour of elements combining ultra-high performance fibre reinforced concretes (UHPFRC) and reinforced concrete', *PhD-Thesis.* (2004) EPFL.
[8] Müller, T., 'Untersuchungen zum Biegetragverhalten von Stahlfaserbeton und betonstahl-bewehrtem Stahlfaserbeton ', *PhD-Thesis.* (2015) HTWL Leipzig.
[9] Haji-Akbari, A., Engel, M., Keys, A., Zheng, X., Petschek, R., Paly-Muhoray, P. and Glotzer, S., 'Disordered, quasicrystalline and crystalline phases of densely packed tetrahedra', *Nature.* (2009).
[10] Hadl, P., 'Zum besseren Verständnis der Streuung des Zugtragverhaltens von stahlfaserbewehrtem Normalbeton und Ultra-Hochleistungsbeton', *PhD-Thesis.* (2017) TU Graz.
[11] Laranjeira, F., Grünewald, S., Walraven, J., Blom, C., Molins, C. and Aguado, A., 'Characterization of the orientation profile of steel fibre reinforced concrete', *Materials and Structures.* **44** (2011) 1093-1111.
[12] Pfyl, T., 'Tragverhalten von Stahlfaserbeton', *PhD-Thesis.* (2003) ETH Zürich.
[13] Leutbecher, T., 'Zum Tragverhalten von zugbeanspruchten Bauteilen aus Ultra-Hochleistungs-Faserbeton', *PhD-Thesis.* (2007) TU Kassel.
[14] CEB-fib, 'Model Code for Concrete Structures 1990', (fib, 1993).
[15] Ma, J., 'Faserfreier Ultrahochfester Beton - Entwicklung und Materialeigenschaften', *PhD-Thesis.* (2010) HTWK Leipzig.
[16] Gröger, J., ' Ein Beitrag zur Beschreibung des Zugtragverhaltens von stahlfaserverstärktem Beton', *PhD-Thesis in preparation.* (2017) HTWK Leipzig.
[17] Jungwirth, J., 'Zum Tragverhalten von zugbeanspruchten Bauteilen aus Ultra-Hochleistungs-Faserbeton', *PhD-Thesis.* (2006) TU München.
[18] Hadl, P., Kim, H., Tue, N.-V., 'Experimental Investigations on the Scattering in the post cracking tensile behavior of UHPFRC', in 'Proceedings of HiperMat 2016', Kassel, March 2016.
[19] Baby, F., Graybeal, B., Marchand, P. and Toutlemonde, F., 'UHPFRC tensile behaviour characterization: inverse analysis of four-point bending test results', *Materials and Structures.* **46** (2013) 1337-1354.
[20] Qian, S. and Li, V., 'Simplified Inverse Method for Determining the Tensile Properties of SHCCs', *Journal of Advanced Concrete Technology.* **6** (2008) 353-363.